Electronic Supplementary Material (ESI) for Materials Horizons.
This journal is © The Royal Society of Chemistry 2014

Electronic Supplementary Information

Strong and Tough Micro/Nanostructured Poly(lactic acid) by Mimicking the Multifunctional Hierarchy of Shell

Huan Xu,[‡a] Lan Xie,[‡a] Jing-Bin Chen,[a] Xin Jiang,[a]

Benjamin S. Hsiao,[b] Gan-Ji Zhong,*[a] Qiang Fu[a] and Zhong-Ming Li*[a]

[a] State Key Laboratory of Polymer Materials Engineering, College of Polymer Science and Engineering, Sichuan University, Chengdu, 610065, Sichuan, People's Republic of China

[b] Department of Chemistry, Stony Brook University, Stony Brook, New York 11794-3400, United States

‡ These authors contributed equally to this work.

Table of Contents

EXPERIMENTAL SECTION

Materials. Commercially available PLA comprising around 2% D-LA was purchased from Nature Works (trade name 4032D). Its weight-average molecular weight and number-average molecular weight were 2.23×10^5 g/mol and 1.06×10^5 g/mol, respectively. Tetrapod-shaped zinc oxide (ZnO) whiskers in the appearance of white powders were custom-made at Chengdu Crystrealm Co. Ltd., China. Taking advantage of the equilibrium gas expanding method, the whiskers were synthesized from metallic zinc as the main raw material without any catalysts. The growth time and temperature were specifically controlled to achieve an extremely wide distribution of the whisker diameter ranging from tens of micrometer to several nanometers.[1] Direct scanning electronic microscopy (SEM) observation of the ZnO whiskers is presented in Figure S2. The ZnO whiskers have a density of 5.3 g/cm^3 and a melting point over 1800 °C. Moreover, the tensile strength and Young's modulus of the ZnO whiskers are 10 GPa and 350 GPa, respectively. Native shells were obtained from local supermarket.

Sample Preparation. PLA composites containing 5 and 10 wt% ZnO whiskers were fabricated by extrusion compounding followed by injection molding, while pure PLA subjected to the same processing conditions was also prepared to make blank control samples. In order to avoid the degradation due to hydrolysis and prevent the formation of voids during processing, ZnO whiskers, PLA and their blends were dried at 100 °C under vacuum overnight before extrusion or injection molding. The compounding process was carried out in a co-rotating twin screw extruder with a ratio of screw length to its diameter (L/D) of 40. Temperatures in seven zones were set at 120, 160, 170, 170, 170, 165, and 165 °C from feed

section to metering section, respectively, and the screw speed was constantly held at 150 rpm, in order to achieve stable melt flow and avoid thermal degradation of PLA. The whisker powders were fed into another port located in barrel of section 3 after the melting of PLA, and the whisker contents in composites were fixed at 5 and 10 wt%, which were adjusted by the feeding speed of PLA and ZnO whiskers.

The dried extruded pellets were injection molded into standard double-bone test samples. The barrel temperature profiles were set at 130, 160, 180, 185, and 180 °C from hopper to nozzle, respectively. The key feature in our strategy involves the utility of a modified injection molding, namely oscillation shear injection molding (OSIM) technique. During packing stage of injection molding process, a controlled shear flow was continuously imposed on the melt by using OSIM technique, which had two hydraulically actuated pistons that move reciprocally at the same frequency of 0.3 Hz and the pressure of 15 MPa. The shear flow did not cease until the gate of the mold solidified. Detailed information of the OSIM machine is described in Figures S2-S4. Without applying the oscillation shear, corresponding counterparts were prepared by conventional injection molding (CIM). It should be noticeable that the control samples of neat PLA and PLA composites containing 5 and 10 wt% of ZnO whiskers subjected to the same thermal conditions were also prepared (i.e., the case without oscillation shear flow). The composites loaded higher contents of whiskers (e.g., 20 wt%) were, unfortunately, characterized by poor processability. We failed to successfully accomplish the injection molding (neither OSIM nor CIM), although we were able to obtain the compounds during the extrusion. The cycle time of the sample preparation by OSIM and CIM was fixed at about 3 min in this study. The mold temperature was held at

50 °C with the aid of an automatic temperature control system during the whole cycles for both OSIM and CIM processing. The abbreviations of normal PLA and structured PLA follow the presentation shown in the main text, while others are designated by the processing method and filler content, i.e., OSIM PLA, CIM PLA5, OSIM PLA5 and CIM PLA10. For instance, normal PLA represents the sample of pure PLA molded by CIM, OSIM PLA5 is the PLA composite loaded 5 wt% ZnO whiskers molded by CIM, while CIM PLA10 and structured PLA stand for the sample of PLA composite containing 10 wt% ZnO whiskers prepared by CIM and OSIM, respectively. The thickness of the injection-molded samples is 4 mm.

Characterization and Testing.

Scanning Electronic Microscopy (SEM). To get a clear observation of the morphology of the crystalline superstructures and whiskers in the injection-molded samples, a small block was cut from the injection-molded part firstly, and then the block was cryogenically fractured along the midcourt line in the flow direction after freezing in liquid nitrogen for 0.5h. The as-obtained fracture surfaces were directly used for the observation of the morphology of ZnO whiskers, mainly regarding the dispersion, distribution and alignment in the PLA matrix. The fracture surfaces were moreover etched for the observation of the morphology of crystalline superstructures formed at whiskers and in the bulk. The etching treatment was performed by immersing the fracture surfaces in a water-methanol (1:2 by volume) solution containing 0.025 mol/L of sodium hydroxide for 12 hours at 25 °C, followed by ultrasonic cleaning in distilled water. Herein we were mainly concerned with the crystalline morphology formed in the oriented layer that is 400~800 μm far from the surface of the injection-molded parts of

PLA composites, because the oriented layer normally presents the highest shear strength which tends to induce rich crystalline structures. The core layer (1600~2000 μm) was also observed to obtain the counterparts. To observe the internal biological structure, the shells were cryogenically fractured along two directions after freezing in liquid nitrogen for 0.5h. A field-emission SEM (Inspect F, FEI, Finland), performed with the accelerated voltage of 5 kV, was utilized for all samples. The samples were sputter-coated with gold before observations.

Two-Dimensional Small-Angle X-Ray Scattering (2D-SAXS). 2D-SAXS measurements were conducted at the beamline BL16B1 of Shanghai Synchrotron Radiation Facility (SSRF, Shanghai, China) to examine the crystalline superstructure of PLA in the oriented layer of injection-molded composites, and the explicit sample preparation is presented in our previous work.[2] The 2D-SAXS images were collected with an X-ray CCD detector (Model Mar165, 2048 × 2048 pixels of 80 × 80 μm^2). The sample-to-detector distance was held at 1900 mm, while the monochromated X-ray beam was operated at a constant wavelength of 0.124 nm. The radically integrated intensities $I(q)$ ($q=4\pi\sin\theta/\lambda$) were obtained for integration in the azimuthal angular range of a whole circle, where 2θ represents the scattering angle and λ represents the wavelength of X-ray. The long period between the adjacent kebabs is calculated using the Bragg equation, $L = 2\pi/q^*$. Here L refers to the long period, and q^* indicates the peak position in the scattering curves.

Differential Scanning Calorimeter (DSC). A DSC Q200 (TA Instruments, America) was used to probe the thermal properties such as melting and crystallization behaviors for PLA and the PLA composites. Samples of the neat PLA and the composites (around 5-6 mg), obtained from the oriented layer of the injection-molded bars, were heated from 30 to 190 °C

at a heating rate of 10 °C/min under nitrogen atmosphere. The samples were subsequently melted at 190 °C for 5 minutes to erase the thermal history, and finally cooled down to 30 °C at a cooling rate of 10 °C/min. The crystallinity (χ_c) was calculated by subtracting the enthalpy of cold crystallization and pre-melt crystallization from the enthalpy of melting by using the Equation 1 presented below.

$$\chi_c = \frac{\Delta H_m - \Delta H_{cc} - \Delta H_{pc}}{\Delta H_m^0} \times 100\% \quad (1)$$

where ΔH_m is the enthalpy of melting for PLA, ΔH_{cc} is the enthalpy of cold crystallization, ΔH_{pc} is the enthalpy of pre-melt crystallization, and ΔH_m^0 is the enthalpy of melting for a 100% crystalline PLA taken as 93.7 J/g.[3]

Mechanical Property Testing. The tensile testing was carried out at room temperature using an Instron universal test instrument (Model 5576, Instron Instruments, America) with a crosshead speed of 5 mm/min and a gauge length of 20 mm (the ASTM standard D638). The notched Izod impact tests were carried out according to the ASTM standard D256-06 at room temperature, the dimension of testing specimens were carefully machined to be 50 mm × 6 mm × 4 mm with a V-notch. A minimum of 6 replicates for each sample were tested at the same conditions, and the average values were presented with standard deviation.

UV-Visible Spectrometry. Changes in the UV-visible spectra were monitored with a Shimadzu UV-2101PC spectrophotometer equipped with an integrating sphere. The UV−visible spectra were recorded from 4 mm plates in reflection mode

Observation of the Biological Hierarchy of Shell

Natural shell presents a micro/nanoscale hierarchical structure and precise inorganic-

organic interface, permitting it to achieve a unique combination of light weight, remarkable strength, and toughness. It has been recognized that stiff, two-dimensional (2D) ceramic platelets and tenacious protein layer alternatively stack into the brick-and-mortar structure of shell. To reveal the 2D constructions hierarchically ordered at multiscales, the internal structure was determined from the two orthogonal directions (sides b and c, Figure S1). From the view of side b, Figure S1b and b' suggests needle-like ceramic phase preferentially orient in one direction. On the orthogonal view of side c, Figure S1c and c' illustrates the closely packed layered ceramic architecture, along with organic minor phase as the tenacious linkage. Obviously, the thin layer of the minor constitute is termed the matrix, it encases the ceramic component on all sides and shows great adherence to the ceramic phase. An important conclusion from the exploration of the internal structure is that the important features of the shell structure shows (1) the existence of a space-filling, layered, and segmented architecture on the micro and nano scales, and (2) the major constituent is a ceramic phase, $CaCO_3$, of a high volume fraction, along with an ultrathin, viscoelastic, and resilient organic constituent (consisting of proteins and possibly other organic materials). The present finding shows us the way to design PLA composites, inspiring us to propose the methodology to mimic the structural configurations of the biological shell system.

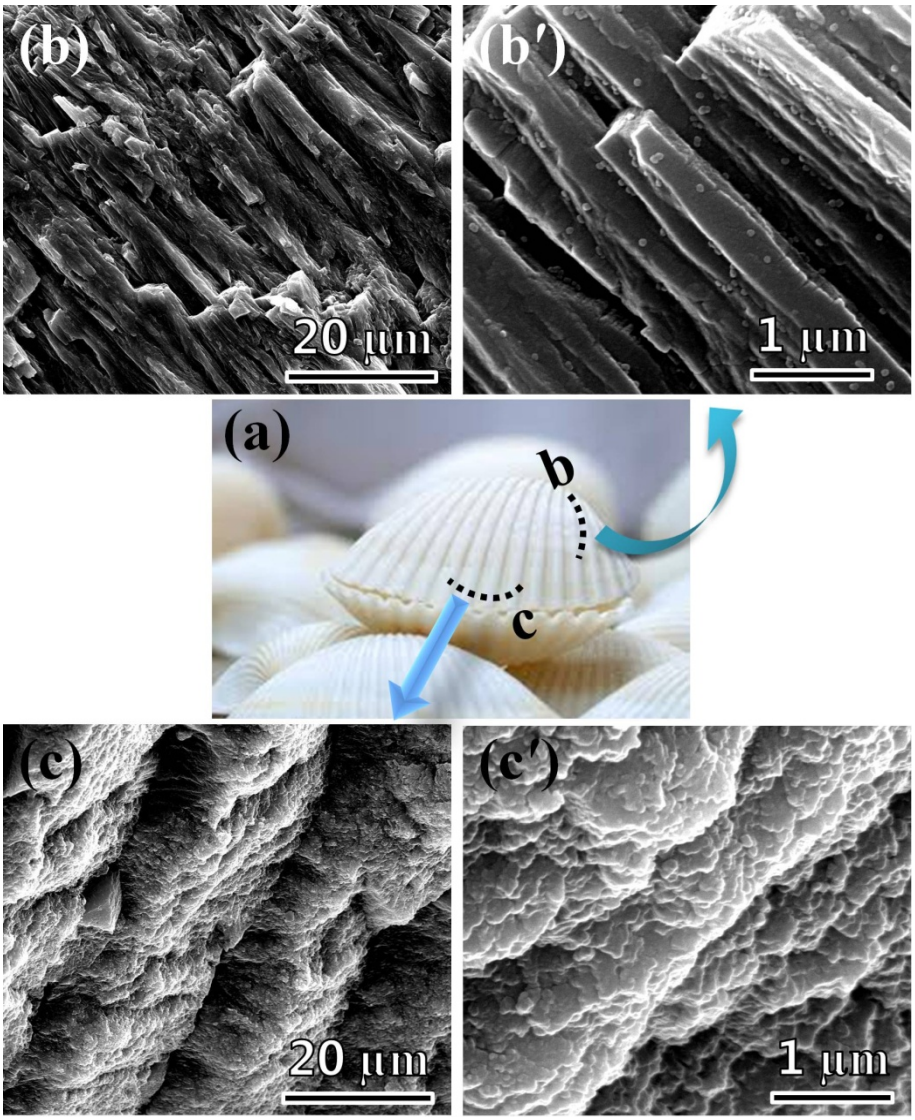

Figure S1. (a) Digital image showing the appearance of the shells used in this work. (b), (c) SEM micrographs showing the architectural configurations of the shell observed from the fracture surfaces as marked in (a).

Morphology of Raw ZnO Whiskers

Figure S2 offers the SEM observation of the morphology of tetrapod-shaped ZnO whiskers. The whiskers were synthesized via equilibrium gas expanding method, and their diameter was customized by specifically controlling the growth time and temperature.[1] The obtained ZnO whiskers are obviously a multiscale mixture system, showing an extremely wide

distribution of diameter ranging from several nanometers to tens of micrometer. In particular, the number of nanowhiskers is fairly equal to that of micro-sized whiskers.

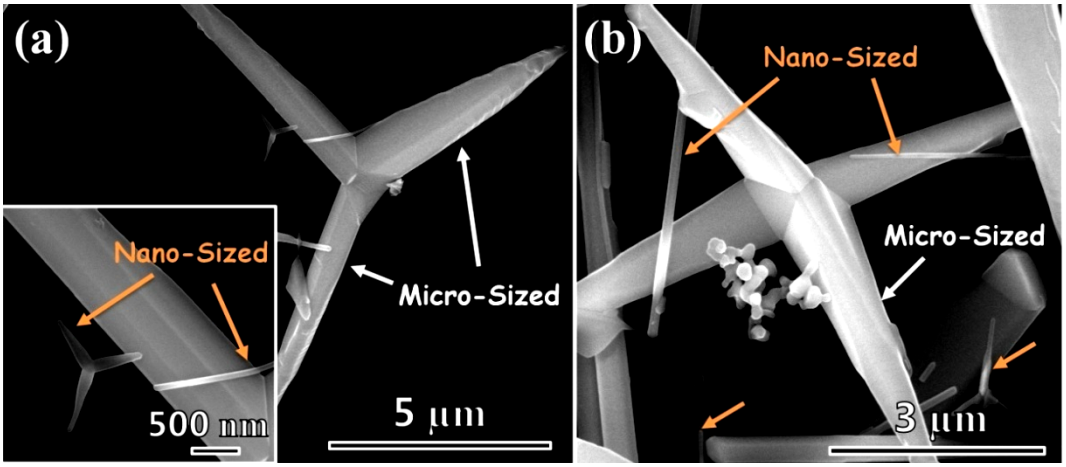

Figure S2. SEM observation of the morphology of raw ZnO whiskers demonstrating the coexistence of micro-sized whiskers and nanowhiskers. The micro-sized whiskers are marked with white arrows in (a) and (b), while the nanowhiskers are marked with orange arrows.

Oscillation Shear Injection Molding (OSIM)

The feature of a melt flow pattern in OSIM is quite different from that of conventional injection molding (CIM), and the crucial difference of the two technologies exists in packing stage, whereas the other stages (i.e., preplasticizing, injection, etc.) are unchanged. The two pistons move out of phase during holding pressure, providing a continuous shear flow field. The shear force would allow the continuous movement of PLA melt that reciprocates in the length direction of moldings, and the shear flow of PLA melt takes place until the gate is solidified. In other words, before being frozen, the PLA melt continuously undergoes repeated shear stress, unless the pistons are stopped. As a result of this, a sufficiently high share rate (over 220 s^{-1}) can impose on the melt in interior region with the increase of the thickness of solidified layer.[4]

Figure S3 shows the digital photograph for the site of OSIM machine, and Figure S4 shows the local picture for the mold with an oscillation shear supplier. The critical point is its mold, whose 3D schematic illustration is shown in Figure S5.

Figure S3. Spot digital photograph showing the OSIM machine.

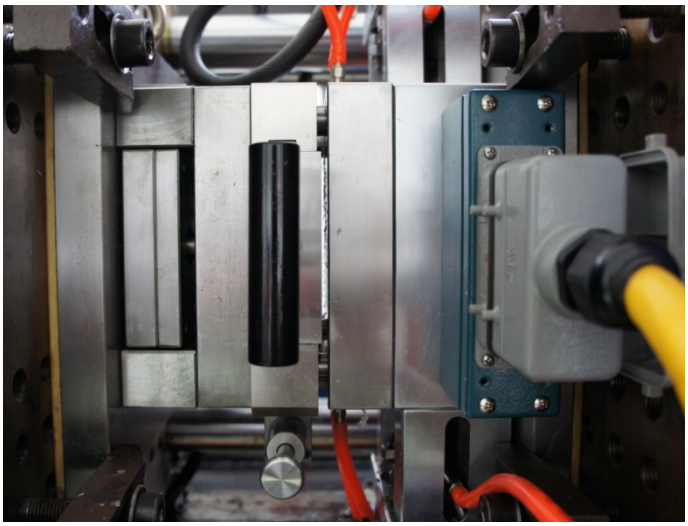

Figure S4. Local picture for the mold with an oscillation shear supplier.

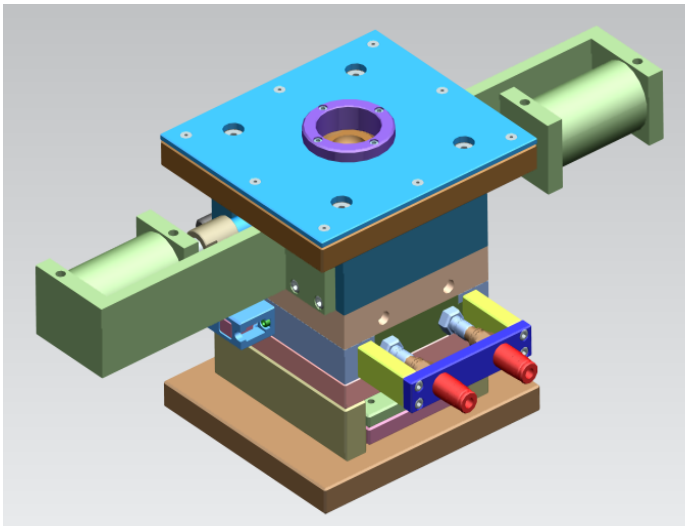

Figure S5. 3D schematic illustration for the mold with an oscillation shear supplier.

Morphology of ZnO Whiskers in the Injection-Molded Bars

Morphology of ZnO whiskers mainly concerning the orientation and dispersion degree in the injection-molded bars is appraised from the SEM observation of the cryogenically fractured surfaces (one indicates the plane along the flow direction, and the other represents the plane perpendicular to the flow direction). For the ZnO whiskers existing in the structured PLA sample, Figure S6a and b evidently suggests the whiskers are well dispersed and regularly align along the flow direction. In clear contrast, no trace of well-organized whiskers is tracked in CIM PLA10 as revealed in Figure S6c and d, demonstrating the presumable aggregation and random distribution of the incorporated whiskers.

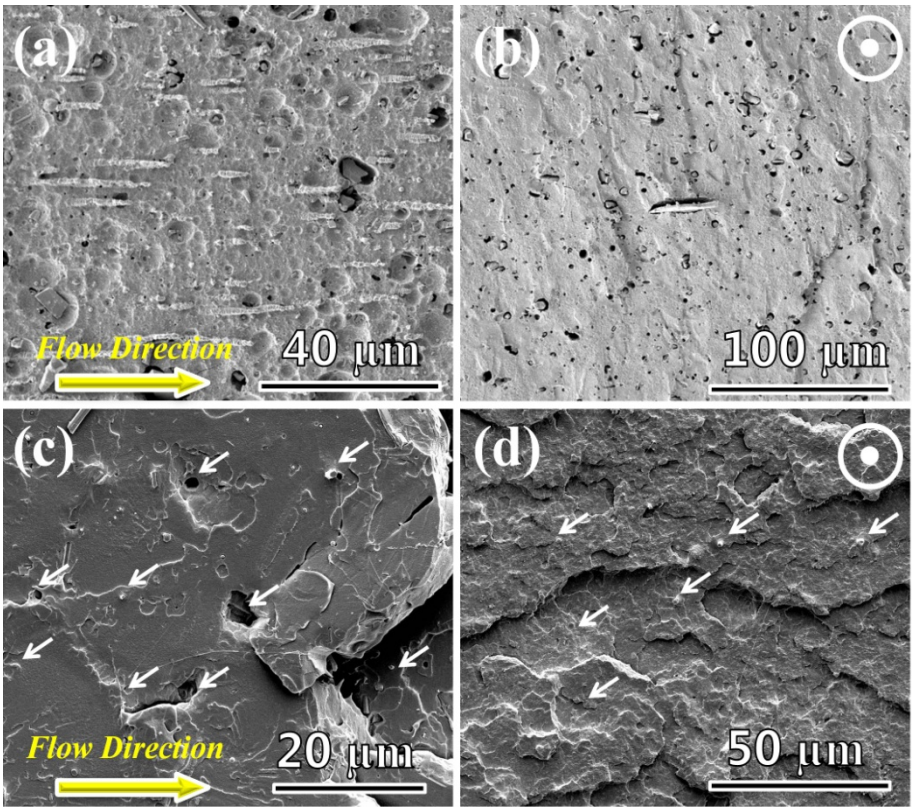

Figure S6. Direct observation of the morphology of whiskers for (a), (b) structured PLA and (c), (d) CIM PLA10. (a) and (c) indicate the plane along the flow direction, while (b) and (d) represent the plane perpendicular to the flow direction. White arrows are marked to point out the whiskers and the holes left by whiskers in CIM PLA10.

Ordered Assemblies of PLA Lamellae in the Structured PLA

Figure S7a offers the direct evidence that the ZnO whisker is decorated with highly ordered lamellae of PLA, as a primary result of the shear-induced oriented chains and the anchoring interactions of the whisker. Moreover, Figure S7b distinctly delineates the unusual formation of PLA shish-kebab structure induced by a pair of incredibly straight shish in the center line. These unique shish reach a length of over 7 μm, assembling the symmetrical alignment of vast kebabs (diameter of ~2.2 μm). Apparently this kind of crystalline morphology is similar to the multiple shish structure of polyethylene.[5]

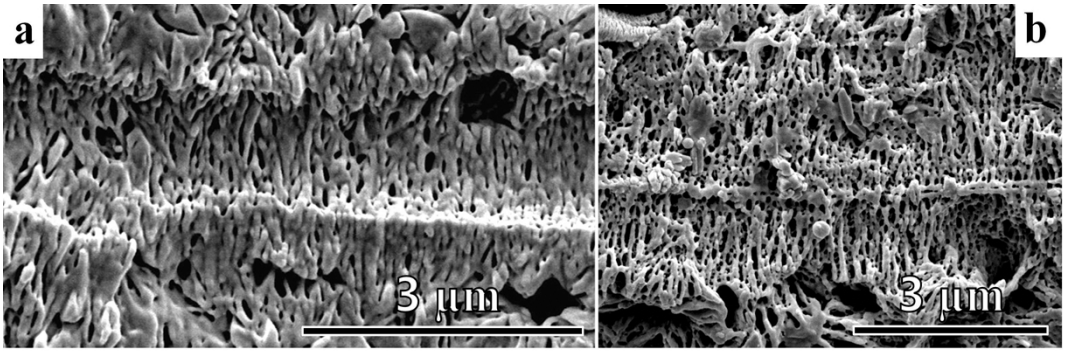

Figure S7. SEM observation of ordered PLA lamellae formed in the oriented layer of structured PLA. (a) Highly aligned lamellae wrapping the micro-sized ZnO whisker, the whisker peeled off from the matrix during the etching process. (b) Shish-kebab superstructure induced by multiple shish in the bulk.

Rich Crystalline Superstructures Formed in OSIM PLA5

Multiple shish structure, transcrystallinity located at the micro-sized whisker, and hybrid shish-kebab of PLA induced by nanowhisker are also observed in the OSIM PLA5 sample, as illustrated in Figure S8a-d. Particularly, Figure S8e schematically emphasizes on the formation mechanism of the multiple shish structure generated in the sheared bulk PLA. The stretch and deformation of entangled chain networks are responsible for this transition of crystalline superstructure under the shear flow. Specifically, the entangled points existing in the shish cannot be unlocked, simultaneously triggering the development of adjacent kebabs.[6]

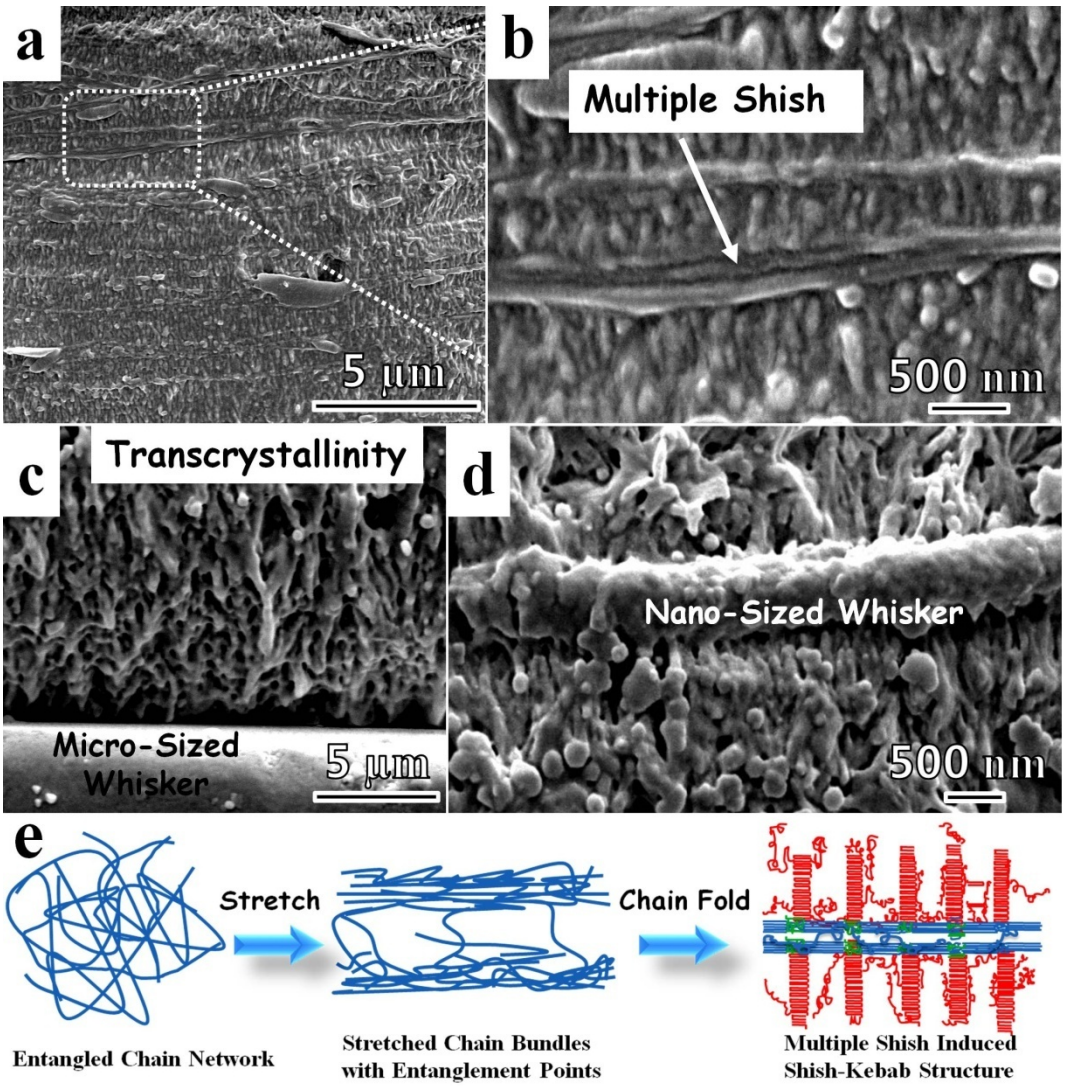

Figure S8. SEM observation of diverse crystalline superstructures formed in the oriented layer of OSIM PLA5. (a) Shish-kebab superstructure induced by multiple shish in the bulk, and (b) in a higher magnification clearly shows the local structure of the multiple shish. (c) Typical transcrystallinity grown at the surface of a micro-sized ZnO whisker. (d) Hybrid shish-kebab superstructure induced by a nanowhisker. (e) Schematic representation of the formation mechanism of multiple shish under the intensive shear flow, the highly oriented multiple shish subsequently induces the symmetrical development of kebabs perpendicular to the shish.

Crystalline Morphology Developed in the Core Layer for OSIM PLA5 and Structured PLA

Figure S9a and S9b shows the crystalline morphology of the OSIM PLA5 and structured PLA sample developed in the core layer, respectively. Obviously, in the core layer only spherulitic texture is presented for both OSIM PLA5 and structured PLA. In contrast to the ordered transcrystallinity and hybrid shish-kebab observed at the whiskers in the oriented layer, there exists only a few polished whiskers in the core layer. The strength of shear flow tends to dramatically decrease along the depth from the surface, attaining the lowest level in the core layer (1600-2000 μm). The shear flow in the core layer is too weak to arouse the transition of spherulites to oriented crystalline superstructures. Without the decoration of ordered lamellae, the interfacial bonding between ZnO whiskers and the PLA matrix must be very poor, leading to the fact that most whiskers may peel off from the PLA matrix and only a small amount of whiskers are traced.

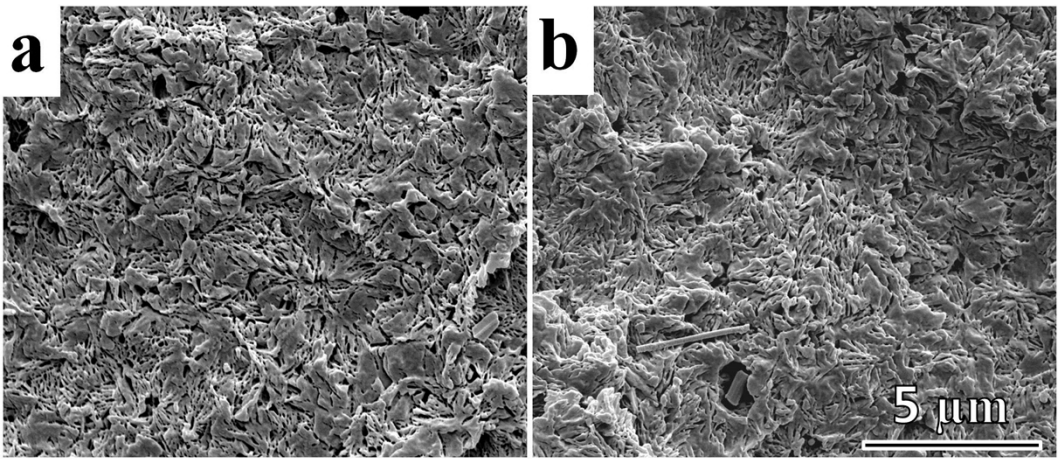

Figure S9. SEM observation of crystalline morphology developed in the core layer of (a) OSIM PLA5 and (b) structured PLA. Only spherulites are observed in both (a) and (b). The scale bar indicates 5 μm for both (a) and (b).

Morphological Observation of CIM Composites

Because PLA is characterized by poor crystallization ability, the CIM processing method featuring weak shear flow is difficult to create obvious crystalline structure for PLA, regardless of the content of ZnO whiskers. Figure S10 describes the crystalline morphology of the CIM PLA5 sample in the oriented layer (Figure S10a and b) and in the core layer (Figure S10c and d). Without the application of an external shear flow, CIM PLA5 is found difficult to develop any form of crystals due to the harsh crystallization conditions during the CIM process (i.e., rapid cooling and weak shear flow). The interfacial bonding between ZnO whiskers and PLA matrix is poor, leading to the presence of many voids rather than whiskers.

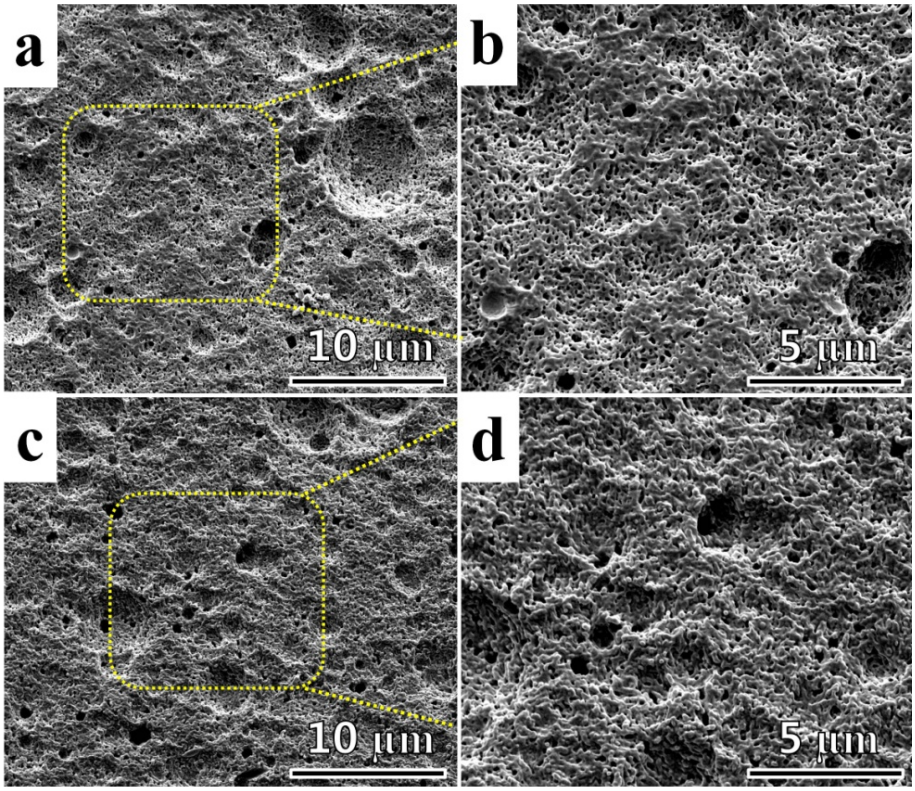

Figure S10. SEM observation of crystalline morphology developed in the (a) oriented layer and (c) core layer of CIM PLA5. (b) and (d) show the local structure in the yellow rectangles of (a) and (c). Neither crystalline texture nor whiskers can be traced in the oriented layer or core layer in the CIM PLA5 sample.

Figure S11 shows the crystalline morphology of the CIM PLA10 sample in the oriented layer (Figure S11a, b) and in the core layer (Figure S11c, d). Like CIM PLA5, no obvious trace of crystals is presented during the CIM process, although the content of ZnO whiskers is increased up to 10 wt%.

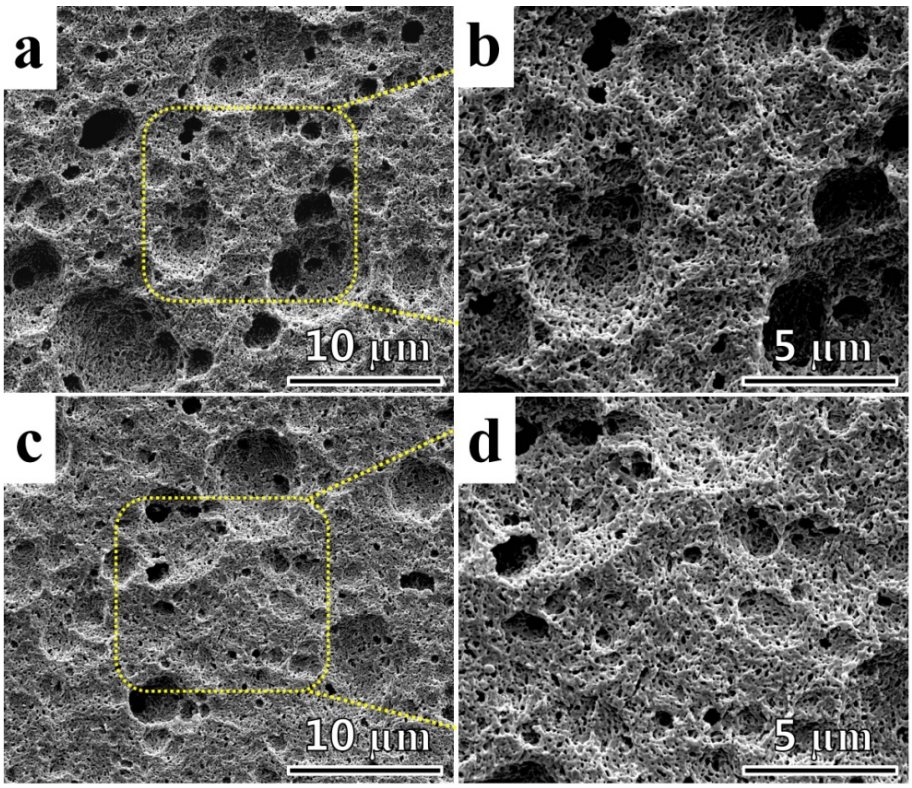

Figure S11. SEM observation of crystalline morphology developed in the (a) oriented layer and (c) core layer of CIM PLA10. (b) and (d) show the local structure in the yellow rectangles of (a) and (c). No crystalline texture is traced in the oriented layer or core layer in the CIM PLA10 sample.

SAXS Determination of Pure PLA and PLA Composites

Figure S12 describes the 2D-SAXS patterns for pure PLA, PLA5 and PLA10 samples processed by CIM and OSIM. The scattering reflection of oriented crystals is observed exclusively for OSIM PLA, OSIM PLA5 and OSIM PLA10, all showing a pair of

symmetrical triangular streaks in the equatorial direction related with the presence of shear-aligned shish and a pair of bulb-shape lobes in the meridional direction associated with the oriented lamellae induced by the shish and whiskers. The 1D-SAXS intensity profiles in Figure S13 produce the long period (L) regarding the lamellar structure.

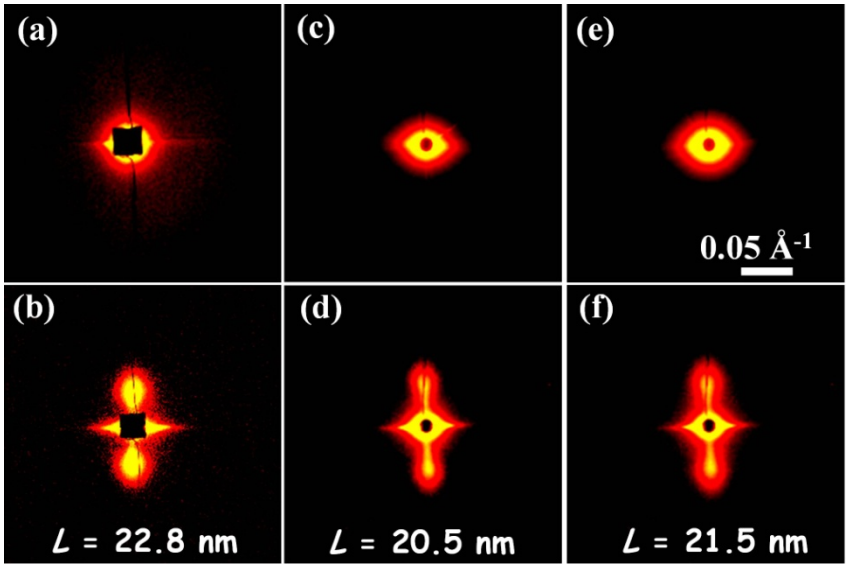

Figure S12. Representative 2D-SAXS patterns of (a) normal PLA, (b) OSIM PLA, (c) CIM PLA5, (d) OSIM PLA5, (e) CIM PLA10 and (f) structured PLA. (b), (d) and (f) evidently suggest the existence of oriented shish-kebab superstructures, and present a long period of 22.8, 20.5 and 21.5 nm, respectively. The q-scale bar is marked in (e).

Figure S13 illustrates the SAXS intensity profiles of the injection-molded pure PLA and composite parts. Apparently, all the OSIM specimens containing shish-kebabs have a maxima around q = 0.3 nm^{-1} in the curves, suggesting a regular aligned lamellar structure with cylindrical symmetry in the shish-kebab, transcrystallinity and hybrid shish-kebab of PLA. In addition, the intensity curves of CIM samples show a monotonically decreasing trend without a maximum. It is likely attributed to the average spacing of lamellar distance with a quite wide distance distribution for the randomly non-oriented lamella morphology in

CIM samples, as evidenced by the SEM observations in Figures S10 and S11. Obviously the SAXS data is well in-line with the SEM observations (Figures S8-11), offering the quantitative information and direct observation for the ordered lamellar alignment of PLA in OSIM samples.

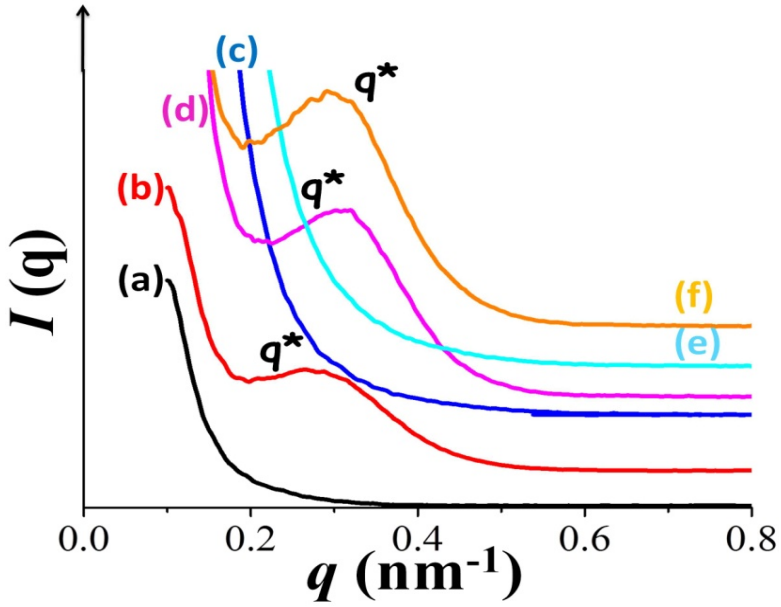

Figure S13. 1-D SAXS intensity profiles of (a) CIM PLA, (b) OSIM PLA, (c) CIM PLA5, (d) OSIM PLA5, (e) CIM PLA10, and (f) structured PLA. Only the OSIM samples show a maxima at around q = 0.3 nm^{-1} in the curves.

Representative Features of 2D-SAXS Patterns for OSIM PLA

One may note that a pair of symmetrical triangular streaks in the equatorial direction were observed in the 2D-SAXS patterns for OSIM PLA and structured composites. It is however difficult to identify them as the indication of shish because they are close to the beamstop. We need to distinguish the scattering patterns from those of CIM PLA and sheared polyolefins. As a representative biodegradable polyester, the shish-kebabs of PLA display the similar appearance with polyolefins (e.g., isotactic polypropylene and polyethylene) (Figure

S14).[2] However, the 2D-SAXS patterns of PLA shish-kebabs show significant difference from those of polyolefins, especially the equatorial streaks suggesting the formation of shish along the flow direction.

Figure S14 compares the 2D-SAXS patterns of sheared PE and sheared PLA (OSIM PE and PLA), as well as the direct morphology of PE shish-kebabs and PLA shish-kebabs from SEM observation. Compared to the tabular streaks of OSIM polyethylene in the equatorial direction, Figure S14a2 suggests a pair of symmetrical triangular streaks for OSIM PLA. The triangular streaks are actually close to the beamstop, however, they cannot originate from the scattering patterns of the beamstop. It is evidenced by the 2D-SAXS patterns of CIM PLA, showing elliptical scattering patterns which are very different from those of OSIM PLA (Figure S14a3). In other words, the 2D-SAXS pattern of CIM PLA is destined to show triangular streaks if the beamstop can arouse the triangular streaks for OSIM PLA.

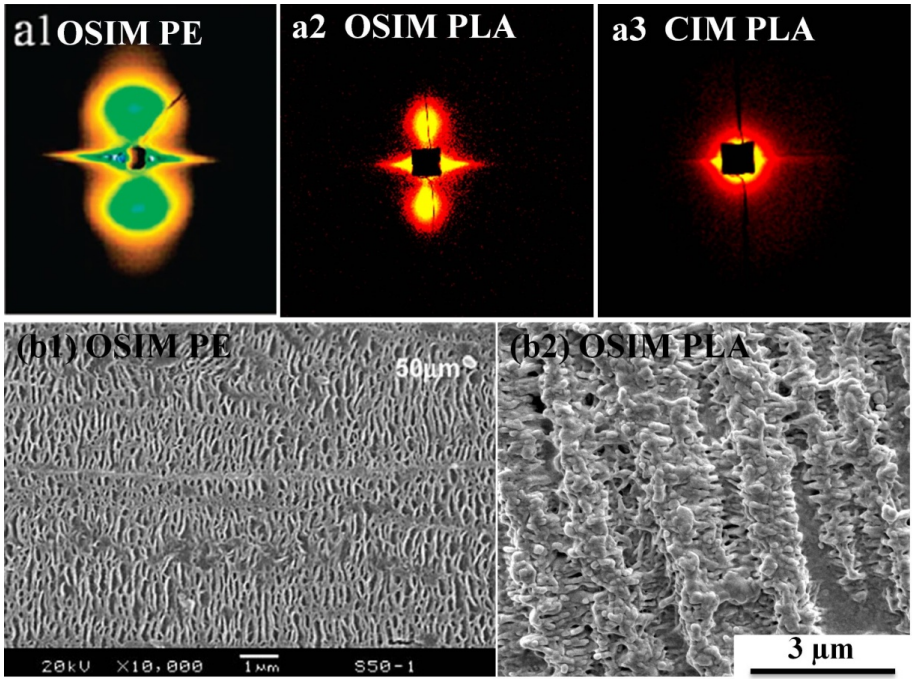

Figure S14. Comparison of the SEM observation and 2D-SAXS patterns for sheared polyethylene (PE) and PLA. (a1) 2D-SAXS patterns of PE reported in Ref. 7; (a2) 2D-SAXS

patterns of sheared PLA in the present work; (a3) 2D-SAXS patterns of CIM PLA in the present work; (b1) SEM observation of PE shish-kebabs reported in Ref. 8; and (b2) SEM observation of PLA shish-kebabs in the present work.

Moreover, it is unusual that the scattering peak corresponding to the steaks cannot be recognized in low q range of 1D-SAXS profile. To examine the origin of equatorial streaks, we attempt to acquire the SAXS profile for the shish separately to confirm the q range of PLA shish. To determine the q range of PLA shish further, we integrated the SAXS patterns of OSIM PLA from -30º to 30º as shown below (Figure S15).

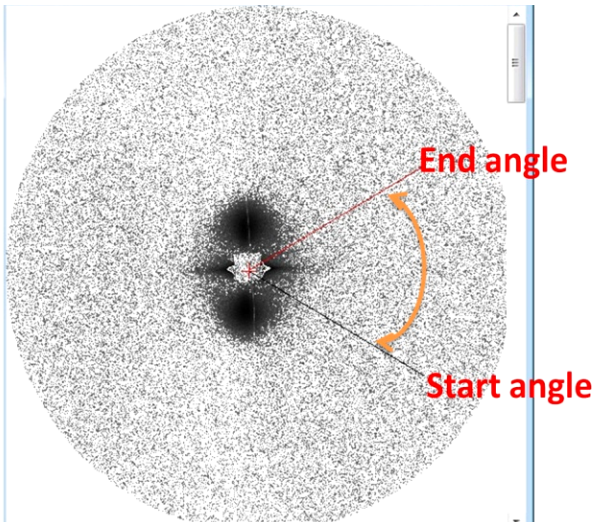

Figure S15. Process window showing the integration of SAXS profiles of OSIM PLA from -30º to 30º.

After the integration, we still cannot detect the clear reflection of equatorial streak as shown in the following curve (Figure S16), which was probably a result of the disturbance of beamstop. In the future, a longer detector-sample distance may be used to avoid this problem.

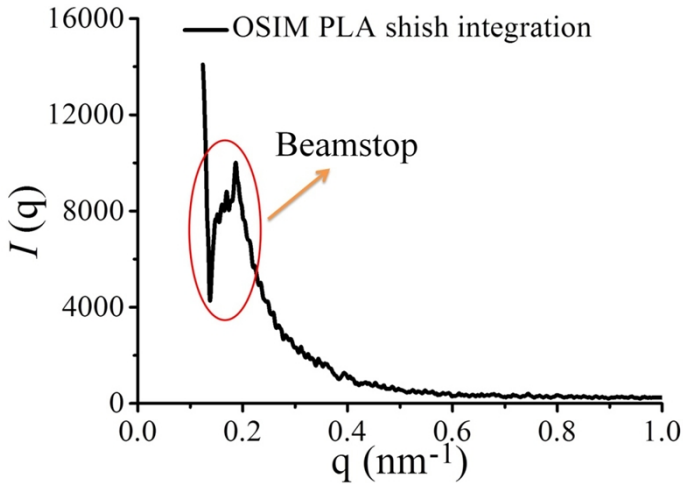

Figure S16. 1D-SAXS curve separately integrated from the PLA shish, only showing the large peak aroused from the beamstop.

Thermal Behaviors of Pure PLA and PLA Composites

Thermal properties of PLA largely rely on the processing history and the molecular interactions of PLA at the whiskers. Figure S17 illustrates the heating process and cooling process of the DSC program, demonstrating the enhanced crystallization ability and crystalline perfection of PLA in the shear flow. And Table S1 collects the detailed thermal properties obtained from DSC heating measurements.

The CIM samples show evident cold crystallization peaks at around 97 °C, which is not observed for OSIM samples (Figure S17A). And the crystallinity is largely increased for OSIM samples (~50%) compared to the fairly low crystallinity of CIM samples (~15%). It indicates the applied shear flow yields relatively perfect crystals and higher crystallinity. Furthermore, the presence of oriented crystalline superstructures gives rise to the obvious enhancement of the melting point, increasing to around 168.5 °C for OSIM samples from the initial 164.5 °C for CIM PLA. Figure S17B reveals the high thermal stability of the oriented

lamellae developed at whiskers. During the cooling process, pure PLA samples do not show any crystallization behavior due to the intrinsically poor crystallization ability of PLA. The distinct melt-crystallization peaks are exclusively observed for PLA composites penetrated ZnO whiskers. Specifically, CIM PLA5 and CIM PLA10 present weak and gentle melt-crystallization peaks at around 98.5 °C. This observation is primarily ascribed to the paramount interactions between the whiskers and PLA, allowing the enhanced occurrence of heterogeneous nucleation.[9] It is of great interest to observe that the crystallization peaks are increased drastically to 118.3 and 107.2 °C for OSIM PLA5 and structured PLA, respectively. The obvious changes of the melt-crystallization peaks for OSIM composites, in essence, stem from the oriented crystalline superstructures generated in the intensive shear. The as-formed lamellae arranged at the surfaces of micro-sized whiskers and nanowhiskers are probably preserved after annealing at 190 °C for 5 min. This must advance the subsequent melt-crystallization during the cooling procedure as these preserved lamellae can absorb and anchor more adjacent chains to pack into lamellar units. It in turn confirms the crucial interactions between the whiskers and PLA, which offers the extremely high thermal stability for these interfacial crystalline superstructures. The combined exploitation of ZnO whiskers and shear flow desirably signifies a promising, versatile strategy to tailor-make oriented PLA lamellae with unusual thermal stability.

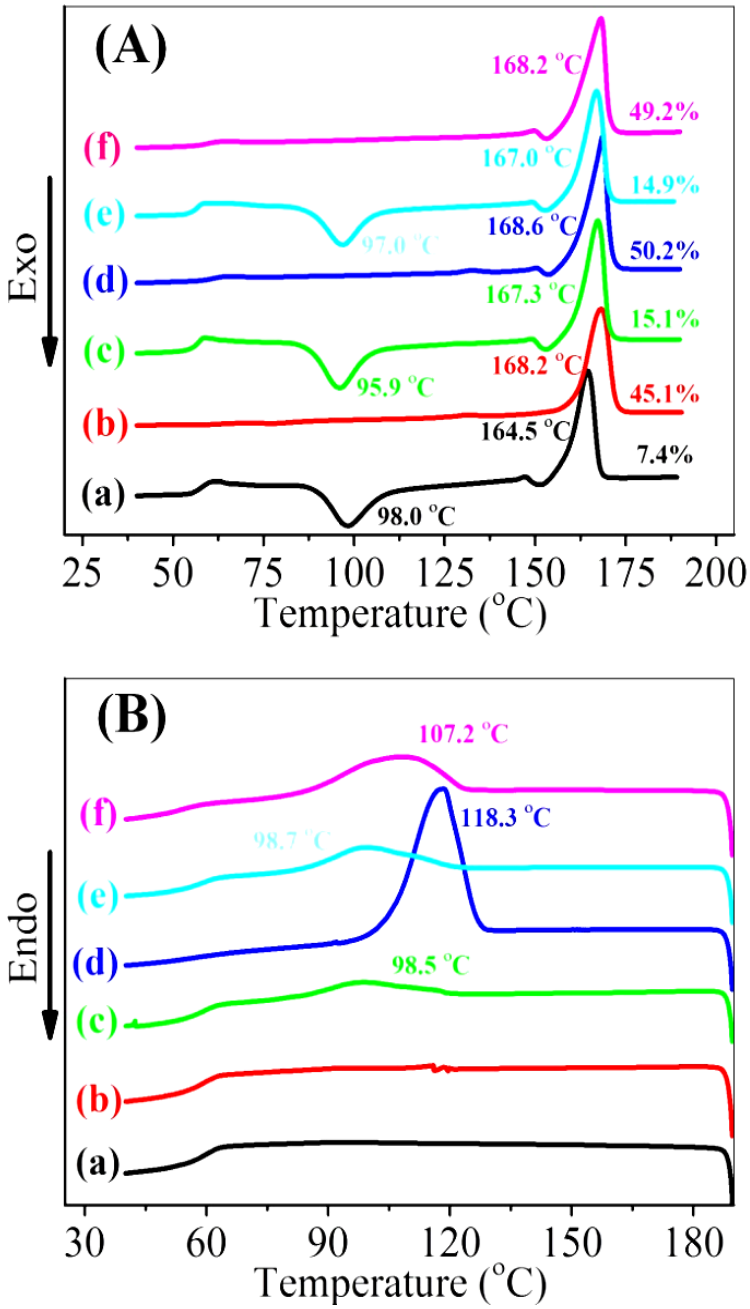

Figure S17. (A) Heating traces and (B) cooling traces of the DSC program of (a) normal PLA, (b) OSIM PLA, (c) CIM PLA5, (d) OSIM PLA5, (e) CIM PLA10, and (f) structured PLA. The cold crystallization temperature (T_{cc}), the melting point (T_m) and crystallinity are marked on the heating traces in (A); the melt crystallization temperature (T_{mc}) is marked on the cooling traces in (B), only PLA/ZnO whisker composites show a melt crystallization peak.

Table S1. Detailed Thermal Properties Obtained from DSC Heating Measurements of

(a) normal PLA, (b) OSIM PLA, (c) CIM PLA5, (d) OSIM PLA5, (e) CIM PLA10, and (f) structured PLA *

	T_g (°C)	T_{cc} (°C)	ΔH_{cc} (J/g)	ΔH_{pc} (J/g)	T_m (°C)	ΔH_m (J/g)	χ_c (%)
a	57.9	98.0	26.4	1.6	164.5	34.9	7.4
b	61.8	-	-	-	168.2	42.3	45.1
c	57.5	96.0	24.3	1.8	167.3	39.6	15.1
d	60.6	-	-	0.5	168.6	44.7	50.2
e	57.1	97.0	23.2	1.8	167.0	37.5	14.9
f	59.7	-	-	0.2	168.2	41.5	49.2

*T_g, the glass transition temperature; T_{cc}, the cold crystallization temperature; T_m, the melting point; ΔH_{cc}, the enthalpy of cold crystallization; ΔH_{pc}, the enthalpy of premelt crystallization; ΔH_m, the enthalpy of melting; χ_c, the crystallinity formed during injection molding. All values of the enthalpy are normalized values based on the matrix content.

Mechanical and Anti-UV Performances of Pure PLA and PLA Composites

Figure S18 describes (A) representative stress-strain curves and (B) UV-visible reflection spectrum for pure PLA and PLA composites containing 5 and 10 wt% ZnO whiskers. And Table S2 gathers the detailed data for the tensile property. The alone addition of whiskers shows weak contribution to the tensile properties, showing moderate improvement of the strength and stiffness. Nevertheless, the shear flow evidently enlarges the reinforcing effects for OSIM PLA5 and structured PLA, achieving the impressive strength of 94.7 and 119.4 MPa, and Young's modulus of 2135 and 2342 MPa, respectively. Moreover, ductility and impact toughness are unusually increased, especially for the multi-fold increase of impact strength as listed in Table S2. Meanwhile, functionalizing PLA with ZnO whiskers will motivate further potential in expanding the application of PLA products,[10–13] e.g., providing

effective shielding of UV light irradiation which undesirably accelerates the photochemical degradation of PLA and therewith deteriorates the physical and chemical properties during the outdoor use.[14] Figure S18B demonstrates the incorporation of ZnO whiskers evidently enables the anti-UV function for PLA. It seems that the shielding efficiency of UV light irradiation relies so little on the content of ZnO whiskers for the composite samples. The OSIM PLA sample, however, is found to give the most interesting results, achieving a remarkably increased absorption of UV light compared to that of CIM PLA. This unexpected improvement in shielding UV light without utilizing additives is interpreted to arise primarily from the formation of rich shish-kebabs in OSIM PLA driven by the intense shear.[2] Despite the invariable component of shish-kebabs, their orientationally ordered lamellar conformation and unique columnar structure may allow them to absorb substantially UV rays in response to light exposure. The present finding creates the potential for realizing the specific anti-UV functionality simply by tailor-making the crystalline superstructure of PLA, in substitution to the normal addition of metallic oxides.[15–17] The enhanced mechanical properties of PLA,[18–20] coupled with the implanted anti-UV functionality[14] and the excellent capability to resist heat deformation,[21,22] desirably provide great possibility to expand the further potential use in biomedical and pharmaceutical devises[23,24] and commodity applications[25] where specific physical and mechanical properties are required.

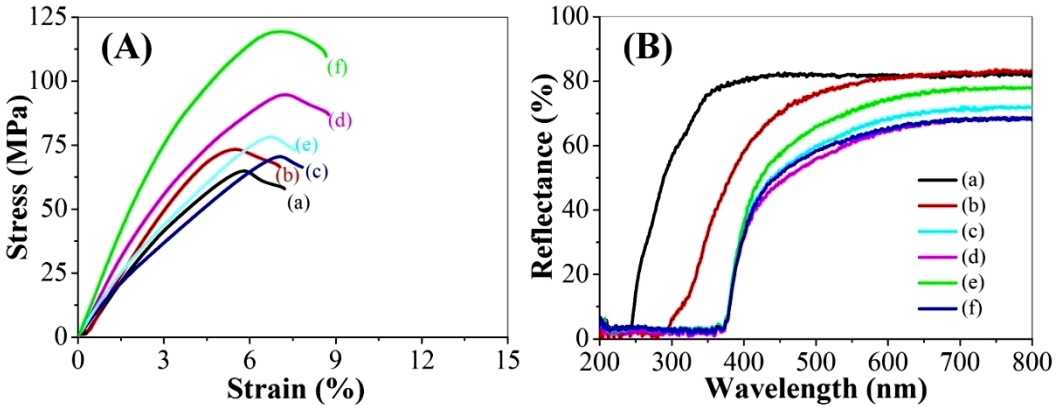

Figure S18. (A) Typical stress-strain curves and (B) UV-visible reflection spectrum of (a) normal PLA, (b) OSIM PLA, (c) CIM PLA5, (d) OSIM PLA5, (e) CIM PLA10, and (f) structured PLA.

Table S2. Detailed Mechanical Properties Obtained from Tensile and Impact Testing of (a) CIM PLA, (b) OSIM PLA, (c) CIM PLA5, (d) OSIM PLA5, (e) CIM PLA10, and (f) structured PLA (results are clarified as average value ± standard deviation after statistical analysis, respectively)

	Tensile Strength (MPa)	Young's Modulus (MPa)	Elongation at Break (%)	Impact Strength (KJ/m^2)
a	64.9±2.6	1684±21	7.3±0.5	4.5±0.3
b	73.7±3.1	1888±33	7.1±0.7	4.2±0.2
c	70.5±2.1	1532±16	7.9±0.3	4.6±0.1
d	94.7±5.3	2135±30	8.8±0.4	7.7±0.5
e	78.3±3.9	1787±23	7.4±0.3	4.9±0.4
f	119.4±6.0	2342±48	8.7±0.5	11.5±0.7

Observation of Tensile Fracture Surfaces for Injection-Molded Composites

The brittle-ductile transition can be observed in OSIM PLA5 like the case of structured PLA (Figure 5), as demonstrated in the SEM images showing the fracture surface after tensile testing (Figure S19). The exploitation of shear flow creates crucial interfacial crystalline

superstructures for PLA composite penetrated micro-sized ZnO whiskers and nanowhiskers. These superstructures enhance the interfacial bonding, allowing plentiful plastic deformation and brittle-ductile transition in favor of mechanical properties. Additionally, Figure S20 demonstrates the intrinsic brittleness of CIM PLA10, as a complementary comparison for the brittle-ductile transition of the structured PLA shown in Figure 5.

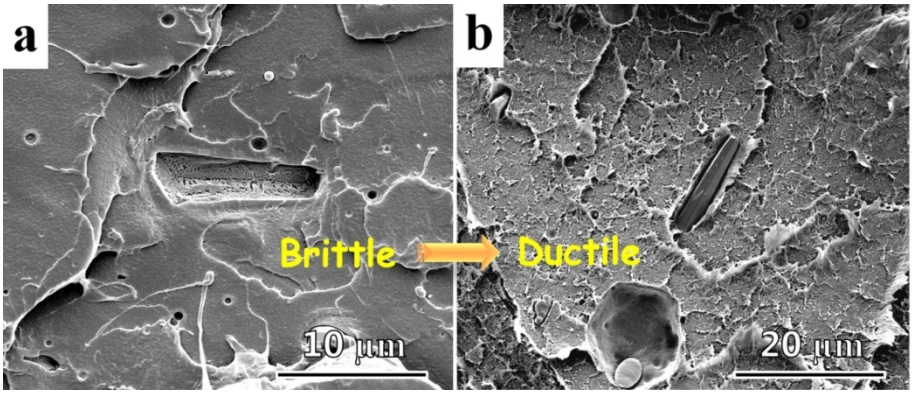

Figure S19. SEM micrographs of fractured surfaces after tensile failure of (a) CIM PLA5 and (b) OSIM PLA5.

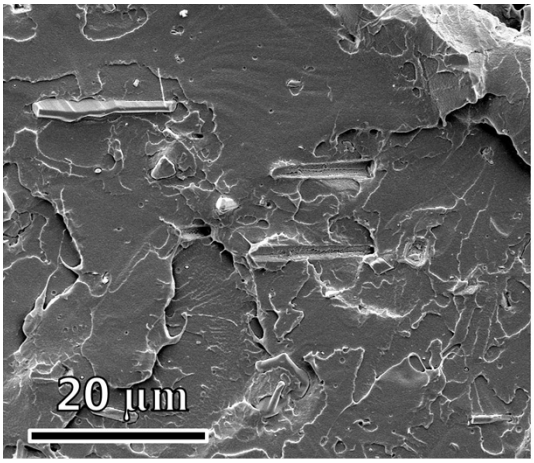

Figure S20. SEM micrographs of fractured surfaces after tensile testing of CIM PLA10.

REFERENCES

1. Fan, X.-M.; Zhou, Z.-W.; Wang, J.; Tian, K. Morphology and Optical Properties of Tetrapod-like Zinc Oxide Whiskers Synthesized via Equilibrium Gas Expanding Method. *Transactions of Nonferrous Metals Society of China* **2011,** *21* (9), 2056-2060.
2. Xu, H.; Zhong, G.-J.; Fu, Q.; Lei, J.; Jiang, W.; Hsiao, B. S.; Li, Z.-M. Formation of Shish-Kebabs in Injection-Molded Poly(l-lactic acid) by Application of an Intense Flow Field. *ACS Applied Materials & Interfaces* **2012,** *4* (12), 6774-6784.
3. Xu, H.; Liu, C.-Y.; Chen, C.; Hsiao, B. S.; Zhong, G.-J.; Li, Z.-M. Easy Alignment and Effective Nucleation Activity of Ramie Fibers in Injection-Molded Poly(lactic acid) Biocomposites. *Biopolymers* **2012,** *97* (10), 825-839.
4. Chen, Y.-H.; Zhong, G.-J.; Wang, Y.; Li, Z.-M.; Li, L. Unusual Tuning of Mechanical Properties of Isotactic Polypropylene Using Counteraction of Shear Flow and *β*-Nucleating Agent on *β*-Form Nucleation. *Macromolecules* **2009,** *42* (12), 4343-4348.
5. Hsiao, B.; Yang, L.; Somani, R.; Avila-Orta, C.; Zhu, L. Unexpected Shish-Kebab Structure in a Sheared Polyethylene Melt. *Physical Review Letters* **2005,** *94* (11), 117802.
6. Yan, T.; Zhao, B.; Cong, Y.; Fang, Y.; Cheng, S.; Li, L.; Pan, G.; Wang, Z.; Li, X.; Bian, F. Critical Strain for Shish-Kebab Formation. *Macromolecules* **2010,** *43* (2), 602-605.
7. Xu, L.; Chen, C.; Zhong, G.-J.; Lei, J.; Xu, J.-Z.; Hsiao, B. S.; Li, Z.-M., Tuning the Superstructure of Ultrahigh-Molecular-Weight Polyethylene/Low-Molecular-Weight Polyethylene Blend for Artificial Joint Application. *ACS Applied Materials & Interfaces* **2012,** *4* (3), 1521-1529.
8. Cao, W.; Wang, K.; Zhang, Q.; Du, R.; Fu, Q., The hierarchy structure and orientation of

high density polyethylene obtained via dynamic packing injection molding. *Polymer* **2006,** *47* (19), 6857-6867.

9. Bussiere, P. O.; Therias, S.; Gardette, J.-L.; Murariu, M.; Dubois, P.; Baba, M. Effect of ZnO Nanofillers Treated with Triethoxy Caprylylsilane on the Isothermal and Non-Isothermal Crystallization of Poly(lactic acid). *Physical Chemistry Chemical Physics* **2012,** *14* (35), 12301.
10. Elumalai, N. K.; Jin, T. M.; Chellappan, V.; Jose, R.; Palaniswamy, S. K.; Jayaraman, S.; Raut, H. K.; Ramakrishna, S. Electrospun ZnO Nanowire Plantations in the Electron Transport Layer for High-Efficiency Inverted Organic Solar Cells. *ACS Applied Materials & Interfaces* **2013,** *5* (19), 9396-9404.
11. Ramsurn, H.; Gupta, R. B. Nanotechnology in Solar and Biofuels. *ACS Sustainable Chemistry & Engineering* **2013,** *1* (7), 779-797.
12. Krebs, F. C.; Norrman, K. Using Light-Induced Thermocleavage in a Roll-to-Roll Process for Polymer Solar Cells†. *ACS Applied Materials & Interfaces* **2010,** *2* (3), 877-887.
13. Therias, S.; Larché, J.-F.; Bussière, P.-O.; Gardette, J.-L.; Murariu, M.; Dubois, P. Photochemical Behavior of Polylactide/ZnO Nanocomposite Films. *Biomacromolecules* **2012,** *13* (10), 3283-3291.
14. Murariu, M.; Doumbia, A.; Bonnaud, L.; Dechief, A. L.; Paint, Y.; Ferreira, M.; Campagne, C.; Devaux, E.; Dubois, P. High-Performance Polylactide/ZnO Nanocomposites Designed for Films and Fibers with Special End-Use Properties. *Biomacromolecules* **2011,** *12* (5), 1762-1771.

15. Yu, H.; Irie, H.; Hashimoto, K. Conduction Band Energy Level Control of Titanium Dioxide: Toward an Efficient Visible-Light-Sensitive Photocatalyst. *Journal of the American Chemical Society* **2010,** *132* (20), 6898-6899.

16. Xiao, J.; Chen, W.; Wang, F.; Du, J. Polymer/TiO_2 Hybrid Nanoparticles with Highly Effective UV-Screening but Eliminated Photocatalytic Activity. *Macromolecules* **2013,** *46* (2), 375-383.

17. Kamada, K.; Tsukahara, S.; Soh, N. Enhanced Ultraviolet Light Tolerance of Peroxidase Intercalated into Titanate Layers. *The Journal of Physical Chemistry C* **2011,** *115* (27), 13232-13235.

18. Ojijo, V.; Sinha Ray, S.; Sadiku, R. Role of Specific Interfacial Area in Controlling Properties of Immiscible Blends of Biodegradable Polylactide and Poly[(butylene succinate)-co-adipate]. *ACS Applied Materials & Interfaces* **2012,** *4* (12), 6690-6701.

19. Ojijo, V.; Sinha Ray, S.; Sadiku, R. Toughening of Biodegradable Polylactide/Poly(butylene succinate-co-adipate) Blends via in Situ Reactive Compatibilization. *ACS Applied Materials & Interfaces* **2013,** *5* (10), 4266-4276.

20. Persson, M.; Lorite, G. S.; Cho, S.-W.; Tuukkanen, J.; Skrifvars, M. Melt Spinning of Poly(lactic acid) and Hydroxyapatite Composite Fibers: Influence of the Filler Content on the Fiber Properties. *ACS Applied Materials & Interfaces* **2013,** *5* (15), 6864-6872.

21. Aou, K.; Kang, S.; Hsu, S. L. Morphological Study on Thermal Shrinkage and Dimensional Stability Associated with Oriented Poly(lactic acid). *Macromolecules* **2005,** *38* (18), 7730-7735.

22. Rahman, N.; Kawai, T.; Matsuba, G.; Nishida, K.; Kanaya, T.; Watanabe, H.; Okamoto,

H.; Kato, M.; Usuki, A.; Matsuda, M.; Nakajima, K.; Honma, N. Effect of Polylactide Stereocomplex on the Crystallization Behavior of Poly(l-lactic acid). *Macromolecules* **2009,** *42* (13), 4739-4745.

23. Zhou, C.; Shi, Q.; Guo, W.; Terrell, L.; Qureshi, A. T.; Hayes, D. J.; Wu, Q. Electrospun Bio-Nanocomposite Scaffolds for Bone Tissue Engineering by Cellulose Nanocrystals Reinforcing Maleic Anhydride Grafted PLA. *ACS Applied Materials & Interfaces* **2013,** *5* (9), 3847-3854.
24. Lahiri, D.; Rouzaud, F.; Namin, S.; Keshri, A. K.; Valdés, J. J.; Kos, L.; Tsoukias, N.; Agarwal, A. Carbon Nanotube Reinforced Polylactide−Caprolactone Copolymer: Mechanical Strengthening and Interaction with Human Osteoblasts in Vitro. *ACS Applied Materials & Interfaces* **2009,** *1* (11), 2470-2476.
25. Xu, X.; Liu, F.; Jiang, L.; Zhu, J. Y.; Haagenson, D.; Wiesenborn, D. P. Cellulose Nanocrystals vs. Cellulose Nanofibrils: A Comparative Study on Their Microstructures and Effects as Polymer Reinforcing Agents. *ACS Applied Materials & Interfaces* **2013,** *5* (8), 2999-3009.